A HIGH-ORDER DOUBLY CONSERVATIVE WEIGHTED ESSENTIALLY NON-OSCILLATORY FINITE VOLUME SCHEME FOR DEGENERATE CONVECTION-DIFFUSION EQUATIONS ON UNSTRUCTURED MESHES*

KAICHANG YU†, JUAN CHENG‡, AND CHI-WANG SHU§

Abstract. Doubly conservative (DoC) schemes, introduced in [Yu, Cheng, Liu, and Shu, *Math. Comp.*, to appear], provide a new framework admitting the Lax-Wendroff type theorem for degenerate convection–diffusion equations. The existing high-order DoC finite volume scheme, however, is largely restricted to uniform meshes, primarily due to the lack of a suitable definition of double cell averages on unstructured meshes. In this work, we introduce a new definition of the double cell average and extend it to non-uniform meshes and unstructured triangular meshes. Based on this definition, we develop a high-order DoC finite volume scheme equipped with weighted essentially non-oscillatory (WENO) reconstruction on non-uniform meshes and unstructured triangular meshes. Extensive numerical experiments validate the high-order accuracy, suppression of spurious oscillations near discontinuities, and robustness of the proposed method.

Key words. non-standard finite volume scheme, high-order methods, degenerate convection-diffusion equations, double conservation, unstructured meshes, weighted essentially non-oscillatory scheme

MSC codes. 65M08, 65M12

1. Introduction.

In this paper, we consider the following two dimensional isotropic convection–diffusion equation with possibly degenerate diffusion:

$$u_t + \nabla \cdot \mathbf{f}(u) = \nabla \cdot (a(u)\nabla u) = \Delta A(u),$$

where $\mathbf{f}(u) = (f_1(u), f_2(u))^\top$, $a(u) \geq 0$ is the non-negative diffusion coefficient and $A(u) = \int^u a(\xi)d\xi$. We will also consider the anisotropic problem later. The degeneracy means that $a(u)$ may be zero, which arises in many applications such as porous media flow and heat transfer [19]. Degenerate convection–diffusion equations typically exhibit free boundaries and even shocks, which pose significant challenges both in analysis and simulation. On the theoretical side, the presence of a free boundary often leads to a loss of regularity. Accordingly, we consider the following ultra-weak solution, which is in $L^1(\mathbb{R}^2 \times \mathbb{R}_+)$ and satisfies the following equation:

$$\iint_{\mathbb{R}_+ \times \mathbb{R}^2} (u\phi_t + \mathbf{f} \cdot \nabla\phi + A\Delta\phi)\, dxdydt = 0, \quad \forall \phi(x, y, t) \in C_0^\infty(\mathbb{R}^2 \times \mathbb{R}_+). \tag{1.1}$$

In the above definition, it is also required that $A(u)$ and components of $\mathbf{f}(u)$ lie in $L^1(\mathbb{R}^2 \times \mathbb{R}_+)$ and are Lipschitz continuous with u.

*Submitted to the editors DATE.

Funding: The work of the second author was partially supported by National Key R&D Program of China No. 2023YFA1009003 and NSFC grant 12571432. The work of the third author was partially supported by NSF grant DMS-2309249.

†Graduate School, China Academy of Engineering Physics, Beijing 100088, China. (yukaichang21@gscaep.ac.cn).

‡Corresponding author. Academy for Multidisciplinary Studies, Capital Normal University, Beijing 100048, China. (jcheng@cnu.edu.cn).

§Division of Applied Mathematics, Brown University, Providence, RI 02912, USA. (chi-wang_shu@brown.edu).

On the numerical side, unlike the hyperbolic conservation laws, for degenerate convection-diffusion equations, even a monotone conservative scheme still may converge to an incorrect solution. This phenomenon was first observed by Evje and Karlsen in 2000 [6]. Then Kadioglu, Nourgaliev and Mousseau reported a similar phenomenon [9]. More recently, Lipnikov, Manzini, Moulton and Shashkov also reported this issue in [11] and identified several schemes which may converge to the wrong solution. Subsequent studies further investigated this phenomenon in [13, 14, 24]. The works mentioned above are limited to second-order accuracy. Most recently, Yu et al. [22] observed a similar phenomenon for a specific local discontinuous Galerkin (LDG) method. They introduced a new conception of "double conservation" and established a Lax-Wendroff type theorem of doubly conservative (DoC) schemes for degenerate convection-diffusion equations to overcome this difficulty. The theorem states that if a sequence of numerical solutions produced by a consistent DoC scheme converges (under suitable bounded-variation assumptions), then its limit is an ultra-weak solution (1.1) of the original equation. This new theorem is suited to high-order numerical schemes and unstructured triangular meshes. The authors also listed several high-order DoC schemes in [22], including DoC-finite difference (DoC-FD) scheme [12], DoC-finite volume (DoC-FV) scheme [23] and DoC-discontinuous Galerkin (DoC-DG) schemes [2, 4].

In this paper, we will focus on the DoC-FV scheme. This scheme was first introduced in [23] and also referred to as the "Zhang–Liu–Shu (ZLS) finite volume scheme" or the "non-standard finite volume scheme". In contrast to conventional finite volume methods, the DoC-FV scheme evolves the double cell average (DCA) rather than the standard cell average. This distinctive formulation endows the scheme with weak monotonicity and allows it to be interpreted as a natural generalization of the DoC-FD scheme [12]. Both schemes employ a similar weighted essentially non-oscillatory (WENO) reconstruction [18] to achieve high-order accuracy in smooth areas and suppress numerical oscillations near sharp interfaces and discontinuities. Subsequent developments of this class of schemes have been reported in, for example, [1, 5, 8, 21]. However, all existing works are restricted to uniform meshes. The primary difficulty in extending the DoC-FV framework to unstructured meshes lies in the definition of the DCA on triangular meshes, which has long been regarded as a challenge [17, 23]. The objective of this work is to overcome this obstacle and to extend the DoC-FV scheme to non-uniform meshes in 1D and unstructured triangular meshes in 2D. To this end, we develop the DoC-FV framework on such meshes and incorporate a multi-resolution WENO (MR-WENO) reconstruction [25, 26] to circumvent the issue of negative linear weights observed in [12, 23].

The main contributions of this work are summarized as follows: (i) We propose a new definition of the DCA that is compatible with unstructured triangular meshes, and construct a DoC-FV discretization based on this DCA. (ii) We couple the DoC-FV discretization on triangular meshes with a new MR-WENO reconstruction which is based on DCAs, leading to a high-order essentially non-oscillatory scheme that avoids the issue of negative weights in [12, 23]. (iii) We introduce a novel decomposition of the hat function and use it to establish the double conservation property of the proposed scheme on triangular meshes. Compared with the traditional decomposition in [16], the new decomposition yields a simpler and more straightforward implementation. (iv) The proposed DoC-FV scheme is further extended to anisotropic diffusion problems. Extensive numerical experiments demonstrate the accuracy, oscillation control, robustness against convergence to incorrect solutions, and flexibility of the proposed method on irregular computational domains.

The organization of this paper is as follows. In Sec. 2, we present the one-dimensional construction, including the new DCA and the scheme on non-uniform meshes, together with the corresponding MR-WENO reconstruction and the verification of the double conservation property. In Sec. 3, we extend the scheme to two-dimensional unstructured triangular meshes and provide the MR-WENO reconstruction strategy, again verifying double conservation. In Sec. 4, we report comprehensive numerical results. Concluding remarks are given in Sec. 5.

2. DoC-FV scheme for convection-diffusion equations: one dimension.

In this section, we consider the one-dimensional degenerate convection-diffusion equation:

$$u_t + f(u)_x = A(u)_{xx}, \quad (x,t) \in \Omega \times (0,T], \tag{2.1}$$

with the initial condition $u(x,0) = u_0(x)$ and the periodic boundary condition for easiness. We first present the definition of an ultra-weak solution of (2.1)

DEFINITION 2.1 ([22]). *We will call a function u as an ultra-weak solution of (2.1) if: (i) $u \in L^1(\mathbb{R}^2 \times \mathbb{R}_+)$. (ii) Both $f(u)$ and $A(u)$ are Lipschitz continuous of u and in the function space $L^1(\mathbb{R} \times \mathbb{R}_+)$. (iii) For any $\varphi \in C_0^\infty(\mathbb{R}^2)$, the following equation holds:*

$$\int_{\mathbb{R}_+}\int_{\mathbb{R}} (u\varphi_t + f(u)\varphi_x + A(u)\varphi_{xx})dxdt + \int_{\mathbb{R}} u_0\varphi dx = 0. \tag{2.2}$$

Next, we present the construction of the new DoC-FV scheme and verify its double conservation, followed by a WENO reconstruction based on DCAs and a comparison with the original ZLS scheme.

2.1. Construction of the new DoC-FV scheme: one dimension.

To better illustrate our scheme, we start with the linear convection-diffusion equation:

$$u_t + u_x = u_{xx}, \quad (x,t) \in \Omega \times (0,T]. \tag{2.3}$$

Decompose Ω into pieces of non-uniform intervals $\Omega = \cup_j I_j$, where $I_j \triangleq [x_{j-\frac{1}{2}}, x_{j+\frac{1}{2}}]$. Denote h as $\max_j |I_j|$. The piecewise linear hat function $\phi_{j+\frac{1}{2}}(x)$ is defined as follows:

$$\phi_{j+\frac{1}{2}}(x) = \begin{cases} \dfrac{-x + x_{j+\frac{3}{2}}}{\Delta x_{j+1}}, & \text{if } x \in I_{j+1}, \\ \dfrac{x - x_{j-\frac{1}{2}}}{\Delta x_j}, & \text{if } x \in I_j, \end{cases} \qquad \Delta x_j = x_{j+\frac{1}{2}} - x_{j-\frac{1}{2}}. \tag{2.4}$$

Multiplying (2.3) by $\phi_{j+\frac{1}{2}}$, integrating over $I_j \cup I_{j+1}$, and integrating by parts yield:

$$\frac{d}{dt}\bar{\bar{u}}_{j+\frac{1}{2}}(t) = \frac{1}{\int_{I_j \cup I_{j+1}} \phi_{j+\frac{1}{2}} dx} \left(\int_{I_j \cup I_{j+1}} u\partial_x \phi_{j+\frac{1}{2}} dx + \frac{u_{j+\frac{3}{2}} - u_{j+\frac{1}{2}}}{\Delta x_{j+1}} - \frac{u_{j+\frac{1}{2}} - u_{j-\frac{1}{2}}}{\Delta x_j} \right), \tag{2.5}$$

where $u_{j+\frac{1}{2}} = u(x_{j+\frac{1}{2}}, t)$ and $\bar{\bar{u}}_{j+\frac{1}{2}}(t)$ is the DCA defined by

$$\bar{\bar{u}}_{j+\frac{1}{2}}(t) = \frac{\int_{I_j \cup I_{j+1}} u(x,t)\phi_{j+\frac{1}{2}}(x)dx}{\int_{I_j \cup I_{j+1}} \phi_{j+\frac{1}{2}} dx} = \frac{2\left(\int_{x_{j-\frac{1}{2}}}^{x_{j+\frac{1}{2}}} u(x,t)\phi_{j+\frac{1}{2}}(x)dx\right)}{\Delta x_j + \Delta x_{j+1}}. \tag{2.6}$$

Notice that $\partial_x \phi_{j+\frac{1}{2}}(x) = -\frac{1}{\Delta x_{j+1}}$ for $x \in I_{j+1}$ and $\frac{1}{\Delta x_j}$ for $x \in I_j$. Then we can design the semi-discrete numerical scheme as follows:

$$\begin{aligned}\frac{d}{dt}(\bar{\bar{u}}_h)_{j+\frac{1}{2}}(t) =& \frac{2}{\Delta x_j + \Delta x_{j+1}}\Bigg(-\sum_\alpha w_\alpha \left((u_h)_{j+1,\alpha} - (u_h)_{j,\alpha}\right) \\ &+ \frac{(u_h)_{j+\frac{3}{2}} - (u_h)_{j+\frac{1}{2}}}{\Delta x_{j+1}} - \frac{(u_h)_{j+\frac{1}{2}} - (u_h)_{j-\frac{1}{2}}}{\Delta x_j}\Bigg),\end{aligned} \tag{2.7}$$

where u_h is the numerical solution and the upwinding numerical flux $(u_h)_{j,\alpha}$ approximates the point value $u(x_{j,\alpha}, t)$ at the α-th quadrature point $x_{j,\alpha}$ in I_j, satisfying that $\Delta x_j \sum_\alpha w_\alpha (u_h)_{j,\alpha} \approx \int_{I_j} u(x,t)dx$. The exact solution $u(x,t)$ satisfies the equation (2.5), this ensures the compatibility of our scheme. For clarity, we omit the subscript h from u_h and $\bar{\bar{u}}_h$ when no confusion arises. Applying a forward Euler temporal discretization, we can formally immediately get the scheme approximating the equation (2.1) as follows:

$$\frac{\bar{\bar{u}}^{n+1}_{j+\frac{1}{2}} - \bar{\bar{u}}^{n}_{j+\frac{1}{2}}}{\Delta t} = \frac{2}{\Delta x_j + \Delta x_{j+1}}\left(-\sum_\alpha w_\alpha \left(\hat{f}^n_{j+1,\alpha} - \hat{f}^n_{j,\alpha}\right) + \frac{A^n_{j+\frac{3}{2}} - A^n_{j+\frac{1}{2}}}{\Delta x_{j+1}} - \frac{A^n_{j+\frac{1}{2}} - A^n_{j-\frac{1}{2}}}{\Delta x_j}\right), \tag{2.8}$$

where n is a nonnegative integer number, $\bar{\bar{u}}^0_{j+\frac{1}{2}} = \frac{2}{\Delta x_j + \Delta x_{j+1}} \int_{x_{j-\frac{1}{2}}}^{x_{j+\frac{1}{2}}} u_0(x)\phi_{j+\frac{1}{2}}(x)dx$, Δt is the size of time step and the numerical fluxes $\hat{f}^n_{j,\alpha}$ is taken as the Lax-Friedrichs flux:

$$\hat{f}^n_{j,\alpha}(u,v) = \frac{1}{2}\left(f(u) + f(v) - \max_u |f'(u)|(v-u)\right), \tag{2.9}$$

and $A^n_{j+\frac{1}{2}} = A(u^n_h(x_{j+\frac{1}{2}}))$ is the numerical approximation of $A(u(x_{j+\frac{1}{2}}, t^n))$, $u^n_h(x)$ is the numerical solution at time t^n. The evaluation of these quantities is described in Sec. 2.3.

Remark 2.2. This new scheme in one dimension is very similar to the original ZLS scheme, but the difference lies in the definition of the DCA. In the original ZLS scheme, the DCA is defined as the moving average:

$$\bar{\bar{u}}^*_j \triangleq \frac{1}{(\Delta x)^2}\int_{x_{j-\frac{1}{2}}}^{x_{j+\frac{1}{2}}}\int_{x-\frac{\Delta x}{2}}^{x+\frac{\Delta x}{2}} u(\xi)d\xi dx, \tag{2.10}$$

where Δx is the length of the uniform mesh. This definition is equivalent to taking an inner product with the function ϕ_j, which is defined at the cell center:

$$\bar{\bar{u}}^*_j = \frac{1}{\Delta x}\int_{x_{j-1}}^{x_{j+1}} u(x)\phi_j(x)dx, \quad \phi_j(x) = \begin{cases}\dfrac{-x + x_{j+1}}{\Delta x}, & \text{if } x \in [x_j, x_{j+1}],\\ \dfrac{x - x_{j-1}}{\Delta x}, & \text{if } x \in [x_{j-1}, x_j),\end{cases} \tag{2.11}$$

where $x_j = (x_{j-\frac{1}{2}} + x_{j+\frac{1}{2}})/2$. This construction relies heavily on the assumption of uniform meshes (see Fig. 2.1(a)). In contrast, we redefine the DCA at mesh vertices in (2.6) (see Fig. 2.1(b)). This modification removes the uniform-mesh restriction and allows the scheme to be applied to non-uniform and unstructured triangular meshes.

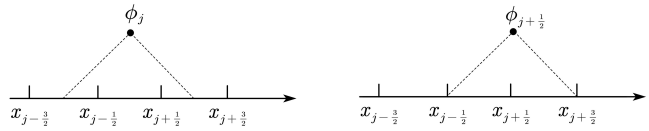

(a) Cell-centered DCA (original ZLS scheme)

(b) Vertex-based DCA (new scheme in this paper)

FIG. 2.1. *Illustration of the DCAs in one dimension.*

2.2. Double conservation: one dimension. As stated before, the nonlinear convective term and the degeneracy of diffusion might generate discontinuities in the solution and will bring challenges in simulation. Building upon the recent work of [22], a Lax–Wendroff-type theorem can be established provided that the fully discrete scheme (2.8) is both DoC and consistent. The relevant definitions and the theorem are stated below.

DEFINITION 2.3 (Double conservation [22]). *A numerical scheme is DoC if it can be written in the following form:*

(2.12)
$$\frac{\tilde{u}_j^{n+1}-\tilde{u}_j^n}{\Delta t}+\frac{\left(\tilde{f}_{j+\frac{1}{2}}^n-\tilde{f}_{j-\frac{1}{2}}^n\right)}{\tilde{x}_{j+\frac{1}{2}}-\tilde{x}_{j-\frac{1}{2}}}=\frac{1}{\tilde{x}_{j+\frac{1}{2}}-\tilde{x}_{j-\frac{1}{2}}}\left(\frac{\tilde{A}_{j+1}^n-\tilde{A}_j^n}{\tilde{x}_{j+1}-\tilde{x}_j}-\frac{\tilde{A}_j^n-\tilde{A}_{j-1}^n}{\tilde{x}_j-\tilde{x}_{j-1}}\right),\ \forall j,n\in\mathbb{N}$$

where $\tilde{u}_j^n$ represents the locally conserved variable, $\tilde{f}_{j+\frac{1}{2}}^n$ and $\tilde{A}_j^n$ are the numerical fluxes. All these tilde-quantities are functions depending locally on the numerical solution $u_h^n(B_j)$, where $B_j=\{x\in\mathbb{R}:|x-\tilde{x}_j|\le ch\}$, with $c>0$ being a positive number independent of the mesh sizes. The tilde grids $\tilde{x}_j$ and $\tilde{x}_{j+\frac{1}{2}}$ are fixed points and depend on the specific scheme.

Before specifying the tilde quantities in our scheme, we recall the general consistency requirements for DoC schemes.

DEFINITION 2.4 (Consistency [22]). *A DoC scheme (2.12) for degenerate convection-diffusion equations* (2.1) *is consistent if the locally conserved variable $\tilde{u}_j^n$ and numerical fluxes $\tilde{f}_{j+\frac{1}{2}}^n$ and $\tilde{A}_j^n$ satisfy:*

(i) If $u_h^n(x)$ is a constant u for all $x\in B_j$, we have

$$\tilde{u}_j^n=u,\quad \tilde{f}_{j+\frac{1}{2}}^n=f(u),\quad \tilde{A}_j^n=A(u).$$

(ii) The tilde-functions are all Lipschitz continuous with respect to the numerical solution, that is, there exists a positive constant $C>0$ such that

$$\left|\tilde{u}_j^n-\tilde{v}_j^n\right|+\left|\tilde{f}_{j+\frac{1}{2}}^n(u_h^n)-\tilde{f}_{j+\frac{1}{2}}^n(v_h^n)\right|+\left|\tilde{A}_j^n(u_h^n)-\tilde{A}_j^n(v_h^n)\right|\le C\|u_h^n-v_h^n\|_{L^\infty(B_j)},\tag{2.13}$$

for any two numerical solutions u_h^n and v_h^n of the scheme and any indices j,n.

(iii) The local conservation could recover global conservation

$$\sum_j|I_j|\tilde{u}_j^n=\int_{\mathbb{R}}u_h^n(x)dx,\ \forall n\ge 0.$$

Now we specify the tilde quantities in our scheme, they are defined as follows:

(2.14)
$$\tilde{u}_j^n=\bar{\bar{u}}_{j+\frac{1}{2}}^n,\ \tilde{f}_{j+\frac{1}{2}}^n=\sum_\alpha w_\alpha\hat{f}_{j+1,\alpha}^n,\ \tilde{A}_j^n=A_{j+\frac{1}{2}}^n,\ \tilde{x}_{j+\frac{1}{2}}=x_{j+1},\ \tilde{x}_j=x_{j+\frac{1}{2}},\ \forall j,n\in\mathbb{N},$$

where $x_{j+1} = \left(x_{j+\frac{1}{2}} + x_{j+\frac{3}{2}}\right)/2$. It is clear that our scheme (2.8) is DoC and consistent. Then under the bounded variation assumptions (see [22] for more details), it will enjoy the following Lax-Wendroff type theorem.

THEOREM 2.5 (Lax-Wendroff type theorem [22]). *Assume that the solution sequence $\{u_h\}$ is generated by a consistent DoC numerical scheme and satisfies the above assumptions, then if the sequence $\{u_h\}$ converges boundedly almost everywhere to some function u as $\tau, h \to 0$, then u is an ultra-weak solution* (2.2) *of the convection-diffusion equation* (2.1).

2.3. DoC MR-WENO reconstruction: one dimension. Achieving high-order accuracy requires precise approximations of the numerical fluxes, with particular emphasis on the reconstruction of the solution values at the quadrature points $u_h^n(x_{j,\alpha})$ and at the cell center $u_h^n(x_j)$. This MR-WENO reconstruction presented here follows the ideas in [25, 26].

(1) **Linear reconstruction.** Given the DCAs $\{\bar{\bar{u}}_{j'+\frac{1}{2}}\}_{j'\in\mathcal{S}_j}$, we construct reconstruction polynomials $q_\ell(x),\ \ell = 1, 2, 3$, on Ω_j using nested stencils such that

$$\frac{1}{\int_{I_i\cup I_{i+1}} \phi_{i+\frac{1}{2}} dx} \int_{I_i\cup I_{i+1}} q_\ell(x)\phi_{i+\frac{1}{2}}(x)dx = \bar{\bar{u}}_{i+\frac{1}{2}}, \quad \forall i \in S_j^{(\ell)},\ \ell = 1, 2, 3. \tag{2.15}$$

The stencils are $S_j^{(1)} = \{j\}$, $S_j^{(2)} = \{j-1, j, j+1\}$, and $S_j^{(3)} = \{j-2, j-1, j, j+1, j+2\}$, with $\mathcal{S}_j = \cup_{\ell=1}^3 S_j^{(\ell)}$, for the first-, third-, fifth-order approximation separately.

(2) **Equivalent expressions.** Following [25], we introduce equivalent representations $\{p_1, p_2, p_3\}$ of $\{q_1, q_2, q_3\}$ by

$$p_1(x) = q_1(x),\ p_2(x) = \frac{1}{\gamma_{2,2}}q_2(x) - \frac{\gamma_{1,2}}{\gamma_{2,2}}p_1(x),\ p_3(x) = \frac{1}{\gamma_{3,3}}q_3(x) - \sum_{\ell=1}^{2}\frac{\gamma_{\ell,3}}{\gamma_{3,3}}p_\ell(x). \tag{2.16}$$

Here $\gamma_{\ell,\ell_2} = \frac{\bar{\gamma}_{\ell,\ell_2}}{\sum_{l=1}^{\ell_2}\bar{\gamma}_{l,\ell_2}}$, in which $\bar{\gamma}_{\ell,\ell_2} = 10^{\ell-1}$ for $\ell = 1, \cdots, \ell_2$ and $\ell_2 = 2, 3$.

(3) **Smoothness indicators.** For $\ell = 2, 3$, the smoothness indicators are defined as follows:

$$\beta_\ell = \frac{1}{2}\sum_{m=1}^{r}\int_{I_j\cup I_{j+1}} |\tilde{I}_j|^{2m-1}\left(\frac{d^m}{dx^m}p_\ell(x)\right)^2 dx, \qquad \ell = 2, 3, \tag{2.17}$$

where $\tilde{I}_j \triangleq [x_j, x_{j+1}]$ and $r = 2(\ell-1)$. For β_1, we take it as 0 for simplicity, which is also followed the same way in (2.17).

(4) **Nonlinear weights.** We define $\tau = \left(\frac{\sum_{\ell=1}^{2}|\beta_3-\beta_\ell|}{2}\right)^2$ and the nonlinear weights are given by

$$\omega_\ell = \frac{\bar{\omega}_\ell}{\sum_{k=1}^{3}\bar{\omega}_k}, \qquad \bar{\omega}_\ell = \gamma_\ell\left(1 + \frac{\tau}{\epsilon+\beta_\ell}\right), \qquad \ell = 1, 2, 3. \tag{2.18}$$

Here ϵ is taken as 10^{-5} in all numerical experiments.

(5) **Final reconstruction.** The final reconstruction is

$$Q(x) = \sum_{\ell=1}^{3}\omega_\ell p_\ell(x).$$

All quadrature values are evaluated from $Q(x)$.

Remark 2.6. In the implementation of (2.8), the numerical convective flux is given as $\hat{f}^n_{j,\alpha} = f(u^{n,-}_{j,\alpha}, u^{n,+}_{j,\alpha})$. The $u^{n,-}_{j,\alpha}$ is taken as the reconstructed point value at point $x_{j,\alpha}$ from $\mathcal{S}_{j-1}$ and $u^{n,+}_{j,\alpha}$ is taken as the reconstructed point value at point $x_{j,\alpha}$ from $\mathcal{S}_j$. The diffusive flux $A^n_{j+\frac{1}{2}}$ is directly taken as the reconstructed value at point $x_{j+\frac{1}{2}}$ from $\mathcal{S}_j$. The numerical integration is performed using a standard three-point Gauss–Legendre quadrature, with weights ω_α and nodes $x_{j,\alpha}$ selected accordingly, ensuring fifth-order accuracy.

Remark 2.7. Since the concept of double conservation is primarily enforced at the level of the spatial discretization, for simplicity we consider the forward Euler scheme for time integration in the preceding analysis in (2.8) and (2.12). In numerical computation, to achieve higher-order accuracy, we employ the third-order strong stability preserving Runge-Kutta (SSPRK) time discretization method (see e.g., [7]): for an ordinary differential equation $u_t = L(u)$, the SSPRK scheme is given as follows:

$$\begin{cases} u^{(1)} = u^n + \Delta t L(u^n), \\ u^{(2)} = \dfrac{3}{4}u^n + \dfrac{1}{4}u^{(1)} + \dfrac{1}{4}\Delta t L(u^{(1)}), \\ u^{n+1} = \dfrac{1}{3}u^n + \dfrac{2}{3}u^{(2)} + \dfrac{2}{3}\Delta t L(u^{(2)}). \end{cases} \tag{2.19}$$

3. DoC-FV scheme for convection-diffusion equation: two dimensions.

In this section, we generalize our new DoC-FV scheme for anisotropic degenerate convection-diffusion equation on unstructured meshes. The equation is given as follows:

$$u_t + \nabla \cdot \mathbf{f}(u) = \sum_{i_1=1}^{2}\sum_{i_2=1}^{2} \partial_{i_1}\partial_{i_2} A_{i_1 i_2}, \tag{3.1}$$

with the initial condition $u(x, y, 0) = u_0(x, y)$ and the periodic boundary condition for easiness, where ∂_1 denotes ∂_x and ∂_2 denotes ∂_y. In the following, we will use the following symbol to simplify the notations $\nabla^2 : \mathbf{A}(u) \triangleq \sum_{i_1=1}^{2}\sum_{i_2=1}^{2} \partial_{i_1}\partial_{i_2} A_{i_1 i_2}$, where $\nabla^2 = \begin{pmatrix} \partial_{xx} & \partial_{xy} \\ \partial_{xy} & \partial_{yy} \end{pmatrix}$, $\mathbf{A}(u) = \begin{pmatrix} A_{11}(u) & A_{12}(u) \\ A_{12}(u) & A_{22}(u) \end{pmatrix}$ is a symmetric matrix and its derivative matrix

$$\mathbf{a}(u) = \begin{pmatrix} A'_{11}(u) & A'_{12}(u) \\ A'_{12}(u) & A'_{22}(u) \end{pmatrix} \tag{3.2}$$

is a symmetric semi-positive matrix. The symbol ":" in (3.1) is the Frobenius product which means that $\mathbf{B} : \mathbf{A} = \sum_{i_1=1}^{2}\sum_{i_2=1}^{2} B_{i_1 i_2} A_{i_1 i_2}$ with $\mathbf{B} = (B_{i_1 i_2})_{2\times 2}$. The degeneracy means that the eigenvalue of $\mathbf{a}(u)$ may be zero. For the equation (3.1), the definition of the ultra-weak solution is given as follows.

Definition 3.1 ([22]). *We call a function u as an ultra-weak solution of* (3.1) *if: (i) $u \in L^1(\mathbb{R}^2 \times \mathbb{R}_+)$. (ii) All components of $\mathbf{f}$ and $\mathbf{A}$ are Lipschitz continuous with respect to u and belong to the function space $L^1(\mathbb{R}^2 \times \mathbb{R}_+)$. (iii) For any $\varphi \in C_0^\infty(\mathbb{R}^3)$, the following equation holds:*

$$\int_{\mathbb{R}_+}\int_{\mathbb{R}^2} (u\varphi_t + \mathbf{f}\cdot\nabla\varphi + \mathbf{A} : \nabla^2\varphi)dxdydt + \int_{\mathbb{R}^2} u_0\varphi dxdy = 0. \tag{3.3}$$

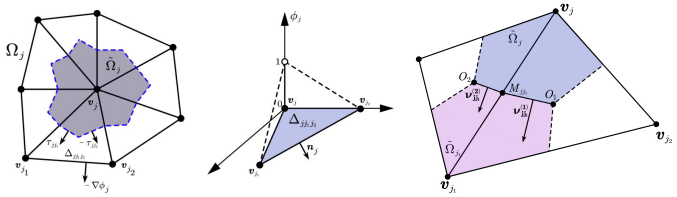

(a) Dual control volume $\tilde{\Omega}_j$ and the hat function ϕ_j on decomposition of $\Delta_{jj_1j_2}$. (b) Barycentric $-\nabla\phi_j$. (c) Intuition geometric interpretation of $\boldsymbol{\nu}$ and dual cells

FIG. 3.1. *The illustration of the dual mesh and barycentric hat function ϕ_j.*

3.1. Construction of the new DoC-FV scheme: two dimensions. Let $\mathcal{T}_h$ be a triangulation of Ω with triangles $\{\Delta_l\}_l$, and let V_l be the vertex set of Δ_l. Given a vertex $\mathbf{v}_j = (x_j, y_j)$, define the triangular set associated with $\mathbf{v}_j$ as $\Omega_j \triangleq \bigcup_{\mathbf{v}_j \in V_l} \Delta_l$, and denote $\widetilde{\Omega}_j$ as the associated vertex-centered dual control volume (the Donald dual mesh, see Fig. 3.1(a)). The set of neighboring vertices of $\mathbf{v}_j$ is denoted as $\mathcal{N}_j$. For any triangle $\Delta_{jj_1j_2} \subset \Omega_j$ with vertices $\mathbf{v}_j$, $\mathbf{v}_{j_1}$ and $\mathbf{v}_{j_2}$ ordered counterclockwise, we define the hat function ϕ_j on $\Delta_{jj_1j_2}$ (see Fig. 3.1(b)) as the barycentric coordinate associated with $\mathbf{v}_j$:

$$\phi_j(x,y)\Big|_{\Delta_{jj_1j_2}} = \mathrm{Det}\begin{vmatrix} x & y & 1 \\ x_{j_1} & y_{j_1} & 1 \\ x_{j_2} & y_{j_2} & 1 \end{vmatrix} \Big/ \left(2\left|\Delta_{jj_1j_2}\right|\right). \tag{3.4}$$

Using the same approach as in the previous section, we test (3.1) with ϕ_j, integrate over Ω_j, and apply elementwise integration by parts to obtain

$$\frac{d}{dt}\int_{\Omega_j} u\,\phi_j + \mathbf{f}(u)\cdot(-\nabla\phi_j)dx\,dy = -\sum_{\Delta_{jj_1j_2}\subset\Omega_j}\int_{\partial\Delta_{jj_1j_2}} (\nabla\phi_j)^\top \mathbf{A}(u)\,\mathbf{n}_j\,ds, \tag{3.5}$$

where $\mathbf{n}_j$ denotes the outward unit normal on $\partial\Delta_{jj_1j_2}$ and $\mathbf{A}(u)\mathbf{n}_j$ denotes the matrix-vector product. Comparing with conventional finite volume methods, the convective term in (3.5) involves an integral over triangles rather than along its boundaries. This raises a practical question of how to incorporate upwinding in the numerical implementation. To this end, we note that $-\nabla\phi_j$ is discontinuous across the boundary $\partial\Delta_{jj_1j_2}$ and, on each $\Delta_{jj_1j_2}$, the gradient $-\nabla\phi_j$ is a constant vector admitting the decomposition:

$$-\nabla\phi_j = \frac{-1}{2|\Delta_{jj_1j_2}|}\begin{pmatrix} y_{j_1}-y_{j_2} \\ -(x_{j_1}-x_{j_2}) \end{pmatrix} = \frac{1}{|\Delta_{jj_1j_2}|}\left(\boldsymbol{\tau}_{jj_1} - \boldsymbol{\tau}_{jj_2}\right), \tag{3.6}$$

where $\boldsymbol{\tau}_{jj_1} = \begin{pmatrix} \frac{y_{j_2}-y_j}{6} + \frac{y_{j_2}-y_{j_1}}{6} \\ -\left(\frac{x_{j_2}-x_j}{6} + \frac{x_{j_2}-x_{j_1}}{6}\right) \end{pmatrix}$, $\boldsymbol{\tau}_{jj_2} = \begin{pmatrix} \frac{y_{j_1}-y_j}{6} + \frac{y_{j_1}-y_{j_2}}{6} \\ -\left(\frac{x_{j_1}-x_j}{6} + \frac{x_{j_1}-x_{j_2}}{6}\right) \end{pmatrix}$. This decomposition (3.6) allows the triangle integrals of the convective term in (3.5) to be reinterpreted as a flux contribution across the boundary of the associated dual control volume $\tilde{\Omega}_j$, thereby enabling the introduction of standard upwind mechanisms on the

dual mesh interfaces. We will explain the usage of this decomposition later. Moreover, the hat function satisfies $\int_{\Omega_j} \phi_j \, dx\, dy = \frac{1}{3}|\Omega_j| = |\widetilde{\Omega}_j|$. We then define the DCA by

$$\bar{\bar{u}}_j \triangleq \frac{1}{|\widetilde{\Omega}_j|}\int_{\Omega_j} u\phi_j dxdy. \tag{3.7}$$

Following (3.5) and (3.6), the scheme can be written as:

$$|\widetilde{\Omega}_j|\left(\frac{\bar{\bar{u}}_j^{n+1}-\bar{\bar{u}}_j^{n}}{\Delta t}\right) = -\sum_{\Delta_{jj_1j_2}\subset\Omega_j}\frac{1}{|\Delta_{jj_1j_2}|}\int_{\Delta_{jj_1j_2}}\Big[\hat{g}(u_j^n,u_{j_1}^n,\boldsymbol{\tau}_{jj_1}) + \hat{g}(u_j^n,u_{j_2}^n,-\boldsymbol{\tau}_{jj_2})\Big]\,dx\,dy - \sum_{\Delta_{jj_1j_2}\subset\Omega_j}\int_{\partial\Delta_{jj_1j_2}}(\nabla\phi_j)^\top\,\hat{\mathbf{A}}\mathbf{n}_j\,ds, \tag{3.8}$$

where $\hat{\mathbf{A}}$ is a matrix-valued numerical flux and $\hat{g}$ is a scalar numerical flux. The values u_i^n $(i=j,j_1,j_2)$ represent the numerical values taken from the side of the vertex $\mathbf{v}_i$. Here and below, $\hat{\mathbf{A}}\mathbf{n}_j$ denotes the matrix-vector product. In implementation, the two integrals appearing in (3.8) are approximated by numerical quadrature. In particular, for each triangle $\Delta_{jj_1j_2}$, we approximate

$$\begin{aligned}&\frac{1}{|\Delta_{jj_1j_2}|}\int_{\Delta_{jj_1j_2}}\Big[\hat{g}(u_j^n,u_{j_1}^n,\boldsymbol{\tau}_{jj_1}) + \hat{g}(u_j^n,u_{j_2}^n,-\boldsymbol{\tau}_{jj_2})\Big]\,dx\,dy\\ \approx&\sum_\alpha w_\alpha\Big[\hat{g}(u_{j,\alpha}^n,u_{j_1,\alpha}^n,\boldsymbol{\tau}_{jj_1}) + \hat{g}(u_{j,\alpha}^n,u_{j_2,\alpha}^n,-\boldsymbol{\tau}_{jj_2})\Big],\end{aligned} \tag{3.9}$$

where $\{w_\alpha,\mathbf{x}_{j,\alpha}\}$ denotes a quadrature rule on $\Delta_{jj_1j_2}$ satisfying that $\sum_\alpha w_\alpha = 1$. Here $u_{j,\alpha}^n$ (resp. $u_{j_m,\alpha}^n$, $m=1,2$) is the one-sided limit of u_h^n at the quadrature point $\mathbf{x}_{j,\alpha}$ taken from the $\mathbf{v}_j$-side (resp. $\mathbf{v}_{j_m}$-side). For the diffusive term, we decompose the boundary $\partial\Delta_{jj_1j_2}$ into its three edges, $\partial\Delta_{jj_1j_2} = \cup_{e=1}^3\partial\Delta_{jj_1j_2}^e$, and let $\mathbf{n}_j^e$ be the unit outward normal to the e-th edge $\partial\Delta_{jj_1j_2}^e$ in $\partial\Delta_{jj_1j_2}$ with respect to $\Delta_{jj_1j_2}$. The boundary integral is then approximated by

$$\int_{\partial\Delta_{jj_1j_2}}(\nabla\phi_j)^\top\,\hat{\mathbf{A}}\mathbf{n}_j\,ds \approx \sum_{e=1}^3\big|\partial\Delta_{jj_1j_2}^e\big|\sum_\beta w_\beta\left((\nabla\phi_j)^\top\,\hat{\mathbf{A}}(u_{j'}^n(\mathbf{x}_\beta^e),u_{j''}^n(\mathbf{x}_\beta^e))\Big|_{\Delta_{jj_1j_2}}\right)\mathbf{n}_j^e, \tag{3.10}$$

where the edge $\partial\Delta_{jj_1j_2}^e$ connects two vertices $\mathbf{v}_{j'}$ and $\mathbf{v}_{j''}$, and $\{w_\beta,\mathbf{x}_\beta^e\}$ denotes a quadrature rule on segment $\overline{\mathbf{v}_{j'}\mathbf{v}_{j''}}$ satisfying that $\sum_\beta w_\beta = 1$. The values $u_{j'}^n(\mathbf{x}_\beta^e)$ and $u_{j''}^n(\mathbf{x}_\beta^e)$ are obtained as the one-sided limits of the numerical solution u_h^n at the quadrature point $\mathbf{x}_\beta^e$, approached from the $\mathbf{v}_{j'}$-side and the $\mathbf{v}_{j''}$-side, respectively. The concrete computations of these one-sided limits (i.e., $u_{j,\alpha}^n$ in (3.9) and $u_{j'}^n(\mathbf{x}_\beta^e)$ in (3.10)) are left in Section 3.3. Together with (3.8) -(3.10), the scheme becomes:

$$\begin{aligned}|\widetilde{\Omega}_j|\left(\frac{\bar{\bar{u}}_j^{n+1}-\bar{\bar{u}}_j^{n}}{\Delta t_n}\right) =& -\sum_{\Delta_{jj_1j_2}\subset\Omega_j}\sum_\alpha w_\alpha\Big[\hat{g}(u_{j,\alpha}^n,u_{j_1,\alpha}^n,\boldsymbol{\tau}_{jj_1}) + \hat{g}(u_{j,\alpha}^n,u_{j_2,\alpha}^n,-\boldsymbol{\tau}_{jj_2})\Big]\\ &-\sum_{\Delta_{jj_1j_2}\subset\Omega_j}\sum_{e=1}^3\big|\partial\Delta_{jj_1j_2}^e\big|\sum_\beta w_\beta\left((\nabla\phi_j)^\top\,\hat{\mathbf{A}}(u_{j'}^n(\mathbf{x}_\beta^e),u_{j''}^n(\mathbf{x}_\beta^e))\Big|_{\Delta_{jj_1j_2}}\right)\mathbf{n}_j^e.\end{aligned} \tag{3.11}$$

The scalar numerical convective flux $\hat{g}(u,v,\boldsymbol{\tau})$ is taken as the Lax-Friedrichs flux:

$$\hat{g}(u,v,\boldsymbol{\tau}) = \frac{1}{2}\left(\mathbf{f}(u)+\mathbf{f}(v)\right)\cdot\boldsymbol{\tau} - \frac{\alpha}{2}(v-u), \qquad \alpha = \max_{u,\boldsymbol{\tau}}\big|\mathbf{f}'(u)\cdot\boldsymbol{\tau}\big|. \tag{3.12}$$

The matrix-valued diffusive flux $\hat{\mathbf{A}}$ is given as

$$\hat{\mathbf{A}}(u,v)=\frac{1}{2}\Big(\mathbf{A}(u)+\mathbf{A}(v)\Big). \tag{3.13}$$

3.2. Double conservation: two dimensions. As in the one dimensional case, the nonlinear convective term and the degeneracy of diffusion may generate low-regularity solutions which will bring challenges of simulation. To address this issue, we employ a Lax-Wendroff type theorem. To this end, we first verify our scheme is DoC and consistent. The notion of DoC schemes on triangular meshes was first introduced in [22]. For simplicity, that work provides a DoC formulation only for the diffusive term, while the convective term is treated by directly adopting the approach proposed in [16]. In particular, the conserved quantity considered in [22] corresponds to the specific dual-mesh setting introduced in [16]. For completeness, we present below the full DoC formulation for the convection–diffusion equation (3.1) under this specific setting.

DEFINITION 3.2 (Double conservation [22]). *A scheme is DoC for the degenerate convection-diffusion equation* (3.1) *if:*

$$\frac{\tilde{u}_j^{n+1}-\tilde{u}_j^n}{\Delta t}+\frac{1}{|\tilde{\Omega}_j|}\sum_{\mathbf{v}_l\in\mathcal{N}_j}\sum_{s=1}^{2}g_{jl}^{(s)}(u_h^n)=-\frac{1}{|\widetilde{\Omega}_j|}\sum_{\Delta_{jj_1j_2}\subset\Omega_j}\int_{\partial\Delta_{jj_1j_2}}\nabla\phi_j^{\top}\tilde{\mathbf{A}}_j ds, \tag{3.14}$$

where $\tilde{u}_j$ is again the locally conserved quantity, the scalar flux $g_{jl}^{(s)}$ and vector-valued flux $\tilde{\mathbf{A}}_j(u_h^n,\mathbf{n}_j)$ are generalized numerical fluxes depended on the numerical solution locally. More precisely, they depend on $u_h^n(B_j)$, where $B_j=\{\mathbf{x}=(x,y)\in\mathbb{R}^2:|\mathbf{x}-\mathbf{v}_j|<ch\}$ with $c>1$ is independent of the mesh size and h is the maximal length of edges in $\mathcal{T}_h$. The index s labels line segments on the cell interface between the dual cells $\tilde{\Omega}_j$ and $\tilde{\Omega}_l$. The function $\phi_j(x,y)$ is the hat function defined in (3.4).

Again, we need the scheme to maintain consistency with the governing equation.

DEFINITION 3.3 (Consistency [22]). *A DoC scheme is consistent if the local conserved quantity and the generalized numerical fluxes satisfy:*

(i) If $u_h^n(\mathbf{x})$ is a constant u, for all $\mathbf{x}\in B_j$, we have:

$$\tilde{u}_j^n(u_h^n)=u,\quad g_{jl}^{(s)}(u_h^n)=\boldsymbol{\nu}_{jl}^{(s)}\cdot\mathbf{f}(u),\quad \tilde{\mathbf{A}}_j(u_h^n,\mathbf{n}_j)=\mathbf{A}(u)\mathbf{n}_j, \tag{3.15}$$

where $\boldsymbol{\nu}_{jl}^{(s)}=|S_{jl}^{(s)}|\mathbf{n}_{jl}^{(s)}$, and $S_{jl}^{(s)}$ is the s-th line segment on the boundary between dual cells $\tilde{\Omega}_j$ and $\tilde{\Omega}_l$. $\mathbf{n}_{jl}^{(s)}$ is the unit outward normal vector on $S_{jl}^{(s)}$ pointing from $\tilde{\Omega}_j$ toward $\tilde{\Omega}_l$. Two unit outward normal vectors are used: $\mathbf{n}_{jl}^{(s)}$, associated with the dual cell $\tilde{\Omega}_j$, and $\mathbf{n}_j$, associated with the triangle $\Delta_{jj_1j_2}$. The vector $\mathbf{n}_j$ is illustrated in Fig. 3.1(b), while a geometric interpretation of $\boldsymbol{\nu}_{jl}^{(s)}$ and the dual cell is shown in Fig. 3.1(c).

(ii) The quantities $g_{jl}^{(s)}$, $\tilde{\mathbf{A}}_j$ and $\tilde{u}_j^n$ are Lipschitz continuous with respect to the numerical solution, that is, there exists a uniform positive constant $C>0$, for all j,n and s, such that

$$|\tilde{u}_j^n-\tilde{v}_j^n|+\Big|g_{jl}^{(s)}(u_h^n)-g_{jl}^{(s)}(v_h^n)\Big|+\sum_{\Delta_{jj_1j_2}\subset\Omega_j}\|\tilde{\mathbf{A}}_j(u_h^n,\mathbf{n}_j)-\tilde{\mathbf{A}}_j(v_h^n,\mathbf{n}_j)\|_\infty\le C\|u_h^n-v_h^n\|_{L^\infty(B_j)}, \tag{3.16}$$

for any two numerical solutions u_h^n and v_h^n, where $\|\cdot\|_\infty$ is the L^∞-norm of a vector. Furthermore, the generalized fluxes $g_{jl}^{(s)}(u_h^n)$ and $\tilde{\mathbf{A}}_j(u_h^n,\mathbf{n})$ should be unique on dual cell interfaces $S_{jl}^{(s)}$ and cell interfaces $\partial\Delta_{jj_1j_2}$ respectively, i.e.,

(3.17)
$$g_{jl}^{(s)}(u_h^n)+g_{lj}^{(s)}(u_h^n)=0,\quad \tilde{\mathbf{A}}_j(u_h^n,\mathbf{n}_j)+\tilde{\mathbf{A}}_j(u_h^n,-\mathbf{n}_j)=0,\ \forall j,\ \mathbf{v}_l\in\mathcal{N}_j,\ s=1,2.$$

(iii) The local conservation could recover global conservation which means

$$\sum_j|\tilde{\Omega}_j|\tilde{u}_j^n=\int_{\mathbb{R}^2}u_h^n(\mathbf{x})d\mathbf{x},\quad \forall n\geq 0.$$

We now verify that our new scheme (3.8) is DoC. We first specify the locally conserved quantity $\tilde{u}_j^n$ and the generalized numerical fluxes $g_{jl}^{(s)}(u_h^n)$ and $\tilde{\mathbf{A}}_j(u_h^n,\mathbf{n}_j)$, in Definition 3.2, as follows:

(3.18)
$$\tilde{u}_j^n=\bar{\bar{u}}_j^n,\ g_{jj_1}^{(1)}=\sum_\alpha w_\alpha\hat{g}(u_{j,\alpha}^n,u_{j_1,\alpha}^n,\boldsymbol{\tau}_{jj_1}),\ g_{jj_2}^{(2)}=\sum_\alpha w_\alpha\hat{g}(u_{j,\alpha}^n,u_{j_2,\alpha}^n,-\boldsymbol{\tau}_{jj_2}),\ \tilde{\mathbf{A}}_j=\hat{\mathbf{A}}\mathbf{n}_j,$$

where the numerical fluxes $\hat{g}$ is given in (3.12), and $\hat{\mathbf{A}}$ is given in (3.13). Then we have the following theorem.

THEOREM 3.4. *The numerical scheme* (3.8) *with* (3.9)-(3.13) *is DoC and consistent.*

Proof. The double conservation follows from the choice of the locally conserved quantity $\tilde{u}_j^n$ and the single-valued property of the generalized numerical fluxes specified in (3.18).

It therefore remains to verify the consistency conditions in Definition 3.3. Conditions (ii) and (iii) are immediate from the construction of the numerical fluxes and the conserved quantity. We thus focus on the exactness on constants stated in equation (3.15). Assume that u_h^n is a constant u, the consistency of $\bar{\bar{u}}_j^n$ and $\hat{\mathbf{A}}_j\mathbf{n}_j$ on constants are immediate. Then it suffices to verify the convective flux identity $g_{jl}^{(s)}(u_h^n)=\boldsymbol{\nu}_{jl}^{(s)}\cdot\mathbf{f}(u)$. We consider $g_{jj_1}^{(1)}$ as an example. Notice that

$$g_{jj_1}^{(1)}(u_h^n)=\mathbf{f}(u)\cdot\boldsymbol{\tau}_{jj_1},\tag{3.19}$$

where the relation $\sum_\alpha w_\alpha=1$ is used. Therefore, to conclude (3.15) for $g_{jj_1}^{(1)}$, it suffices to show that $\boldsymbol{\tau}_{jj_1}=\boldsymbol{\nu}_{jj_1}^{(1)}$, where $\boldsymbol{\nu}_{jj_1}^{(1)}$ is illustrated in Fig. 3.1(c).

Now we aim to prove (3.19). Let O_1 be the barycenter of the triangle $\Delta_{jj_1j_2}$ and let M_{jj_1} be the midpoint of the edge $\overline{\mathbf{v}_j\mathbf{v}_{j_1}}$. Notice that the segment $\overline{O_1M_{jj_1}}$ is the interface segment $S_{jj_1}^{(1)}$ between the dual cells $\tilde{\Omega}_j$ and $\tilde{\Omega}_{j_1}$. Denoting $\mathbf{v}_m=(x_m,y_m)$, we have $O_1=\left(\frac{x_j+x_{j_1}+x_{j_2}}{3},\frac{y_j+y_{j_1}+y_{j_2}}{3}\right)$ and $M_{jj_1}=\left(\frac{x_j+x_{j_1}}{2},\frac{y_j+y_{j_1}}{2}\right)$. Then the vector $\overrightarrow{O_1M_{jj_1}}$ is also given as: $\overrightarrow{O_1M_{jj_1}}=-\left(\frac{x_{j_2}-x_j}{6}+\frac{x_{j_2}-x_{j_1}}{6},\frac{y_{j_2}-y_j}{6}+\frac{y_{j_2}-y_{j_1}}{6}\right)^\top$. By definition, $\boldsymbol{\nu}_{jj_1}^{(1)}$ is the outward normal vector of $\tilde{\Omega}_j$ along $\overline{O_1M_1}$ with length $|\overline{O_1M_1}|$. It is also clear that $\boldsymbol{\tau}_{jj_1}$ is orthogonal to $\overrightarrow{O_1M_{jj_1}}$ and its orientation is fixed by requiring that it points from $\widetilde{\Omega}_j$ to $\widetilde{\Omega}_{j_1}$ by definition (3.6). Since it also have the same length of $\boldsymbol{\nu}_{jj_1}^{(1)}$, we obtain $\boldsymbol{\tau}_{jj_1}=\boldsymbol{\nu}_{jj_1}^{(1)}$. The remaining cases $g_{jj_2}^{(2)}$ and, more generally, $g_{jl}^{(s)}$ follow by the same argument. Then the proof is finished. ∎

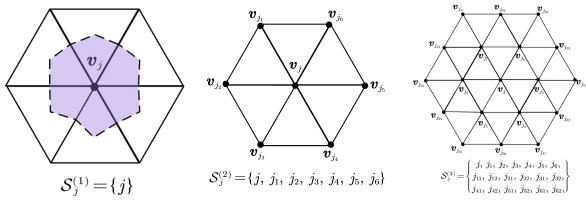

FIG. 3.2. *The illustration of the content of* $S_j^{(i)}$ *with* $i = 1, 2, 3$.

The above theorem relies on the decomposition (3.6) and the equivalence (3.19). Compared with the decomposition in [16], where the constant vector $-\nabla\phi_j$ is expressed as a combination of spatially varying vectors depending on x and y, the present decomposition (3.6) splits the same constant vector into two constant vectors, which significantly simplifies the implementation. Once we prove the new scheme (3.8) is DoC and consistent, then it enjoys the following Lax-Wendroff type theorem.

THEOREM 3.5 (Lax-Wendroff type theorem [22]). *If a sequence of solutions* $\{u_h\}$ *generated by the consistent DoC scheme, with uniformly bounded total variation and support, converges in* L^1 *to a function* u *as* $\tau, h \to 0$*, then* u *is an ultra-weak solution to* (3.1).

3.3. DoC MR-WENO reconstruction: two dimensions. We now describe the new DoC MR-WENO reconstruction based on the DCAs defined in (3.7). This section also follows [25, 26] with appropriate modifications.

(1) **Linear reconstruction**. Given a vertex $\mathbf{v}_j$ and the DCAs $\{\bar{\bar{u}}_{j'}\}_{j'\in\mathcal{S}_j}$, where $\mathcal{S}_j$ denotes the reconstruction stencil of $\mathbf{v}_j$, we construct a hierarchy of reconstruction polynomials on the associated vertex-centered dual control volume Ω_j.
Specifically, we build polynomials of increasing degree using nested stencils: (i) a constant q_1 reconstructed from the DCA on Ω_j, denote $S_j^{(1)} = \{j\}$ and take $q_1 = \bar{\bar{u}}_j^n$; (ii) a quadratic polynomial q_2 reconstructed from the dual cells associated with $\mathbf{v}_j$ and its neighboring vertices, denote the index collection of Ω_l used in this procedure as $S_j^{(2)}$; (iii) a quartic polynomial q_3 reconstructed from an enlarged stencil consisting of $\mathbf{v}_j$, its neighbors, and the neighbors of those neighbors, denote the index collection of Ω_l used in this procedure as $S_j^{(3)}$. Then the $\mathcal{S}_j$ is taken as $\cup_{i=1}^3 S_j^{(i)}$. The illustration of the above procedure is shown in Fig 3.2.
In the above three procedures, if the stencil does not provide a sufficient number of degrees of freedom, it is enlarged by adding one additional layer of neighboring vertices. Conversely, if the number of available degrees of freedom exceeds that required by the reconstruction, a constrained least-squares procedure is employed, subject to the constraint that the DCA over Ω_j is exactly preserved, namely, for $i = 2, 3$,

$$\begin{aligned} &\min_{q_i} \sum_{l\in S_j^{(i)}} \left(\frac{1}{\int_{\Omega_l}\phi_l dxdy} \int_{\Omega_l} q_i(x,y)\phi_l(x,y)dxdy - \bar{\bar{u}}_l \right)^2 \\ &\text{s.t. } \frac{1}{\int_{\Omega_j}\phi_j dxdy} \int_{\Omega_j} q_i(x,y)\phi_j(x,y)dxdy = \bar{\bar{u}}_j. \end{aligned} \tag{3.20}$$

(2) **Equivalent expressions.** The equivalent polynomials $\{p_\ell\}_{\ell=1}^3$ are defined as in

the one-dimensional case (2.16) in Sec. 2.3.

(3) **Smoothness indicators**. The smoothness indicators are computed as follows:

$$\beta_\ell = \frac{1}{|\mathcal{N}_j|}\sum_{|l|=1}^{r}\int_{\Omega_j} |\widetilde{\Omega}_j|^{|l|-1}\left(\frac{\partial^{|l|}}{\partial x^{l_1}\partial y^{l_2}}p_\ell(x,y)\right)^2 dxdy,\ \ell=2,3,\ |l|=l_1+l_2, \tag{3.21}$$

where $r=2(\ell-1)$, l_1 and l_2 are nonnegative integers, and $|\mathcal{N}_j|$ is the number of neighbors of the vertex $\mathbf{v}_j$. Dividing by $|\mathcal{N}_j|$ is introduced to make the resulting weights more comparable to those defined on triangular meshes. Again, we take β_1 as 0.

(4) **Nonlinear weights**. Once we get the $\{\beta_\ell\}_{\ell=1}^3$, the nonlinear weights $\{\omega_\ell\}_{\ell=1}^3$ are defined in the same manner as in (2.18) in Sec. 2.3.

(5) **Final reconstruction**. The final reconstructed approximation of $u(x,y)$ is given by

$$Q(x,y)=\sum_{\ell=1}^{3}\omega_\ell p_\ell(x,y).$$

All the point values $\mathbf{x}_{j,\alpha}, \mathbf{x}_\beta^e$ required in numerical integrals in (3.8)-(3.10) will be taken as $Q(\mathbf{x}_{j,\alpha})$ or $Q(\mathbf{x}_\beta^e)$.

Remark 3.6. For the implementation of (3.8)-(3.10), the $u_{j,\alpha}^n$ in (3.9) is taken as the value $Q(\mathbf{x}_{j,\alpha})$ reconstructed from $\mathcal{S}_j$ and $u_{j'}^n(\mathbf{x}_\beta^e)$ is taken as the value $Q(\mathbf{x}_\beta^e)$ reconstructed from $\mathcal{S}_{j'}$.

Remark 3.7. Similarly with the one dimensional case, the preceding analysis in (3.8) and (3.14) is mainly based on the forward Euler scheme for simplicity. In practice, we replace the forward Euler time scheme in (3.8) with the SSPRK method (2.19) for the time discretization.

4. Numerical experiments.

In this section, we assess the performance of the proposed DoC-FV scheme in both one and two dimensions, especially on unstructured meshes. Most test problems are adopted from the published benchmarks that are widely used in the literature [3, 12, 21, 22]. These problems include the accuracy tests, porous medium type equations and strongly degenerate convection-diffusion equations. We also test the performance of our scheme on irregular domains and anisotropic problems. The time step is chosen according to a CFL-type condition. For one-dimensional problems, we take $\Delta t=\frac{CFL\min_j(\Delta x_j)^2}{\alpha_c\max_j\Delta x_j+\alpha_d}$, where $\alpha_c=\max_u|f'(u)|$ and $\alpha_d=\max_u A'(u)$ in (2.1). For two-dimensional problems, we set $\Delta t=\frac{CFL\min_j|\widetilde{\Omega}_j|}{\alpha_c\sqrt{\max_j|\widetilde{\Omega}_j|}+\alpha_d}$, where $\alpha_c=\max_u(|f_1'(u)|+|f_2'(u)|)$ and α_d is the maximum eigenvalue of the derivative matrix $\mathbf{a}(u)$ defined in (3.2). Through all experiments, we use $CFL=0.4$ following [12, 23].

4.1. 1D numerical results.

We present the results of one dimensional problems, including the accuracy test, porous medium equations (PMEs), Buckley-Leverett equation and strongly degenerate convection-diffusion equations on non-uniform meshes. To construct a non-uniform mesh $\{\hat{x}_{j+\frac{1}{2}}\}_{i=0}^N$, we remain the vertexes $\hat{x}_{\frac{1}{2}}=x_L$ and $\hat{x}_{N+\frac{1}{2}}=x_R$, and perturb the uniform cell interfaces according to

$$\hat{x}_{i+\frac{1}{2}}=x_{i+\frac{1}{2}}+\theta_{i+\frac{1}{2}}\Delta x,\quad \theta_{i+\frac{1}{2}}=0.1\sin\left(2\pi\xi_{i+\frac{1}{2}}\right),\quad i=1,\cdots,N-1, \tag{4.1}$$

where $x_{i+\frac{1}{2}}$ are the interfaces of the underlying uniform grid with spacing Δx, and $\xi_{i+\frac{1}{2}} = \frac{i}{N}$, $i = 1, \cdots, N-1$. It is clear that $\xi_{i+\frac{1}{2}} \in (0,1)$ and $\theta_{i+\frac{1}{2}} \in (0, 0.1)$. In the following, "non-uniform mesh" refers to the meshes generated by (4.1).

4.1.1. Accuracy test: linear convection-diffusion equation. In this test, we solve the following convection-diffusion equation

$$u_t + u_x = \epsilon_d u_{xx}, \tag{4.2}$$

on domain $\Omega = [0, 2\pi]$ with periodic boundary condition. The initial condition is taken as $u_0(x) = \sin(x)$. The equation (4.2) has an exact solution $u(x,t) = e^{-\epsilon_d t}\sin(x-t)$. The ϵ_d is taken as 10^{-3}. We compute the solution up to $T = 1$ on non-uniform meshes. The results are shown in Table 4.1 and demonstrate that our scheme has optimal order of accuracy on non-uniform meshes.

N	L^1 Error	Order	L^2 Error	Order	L^∞ Error	Order
40	1.02e-01	–	7.48e-02	–	1.87e-01	–
80	2.31e-03	5.23	1.27e-03	5.63	1.35e-03	6.81
160	7.22e-05	4.87	3.95e-05	4.88	4.25e-05	4.87
320	2.23e-06	4.95	1.21e-06	4.96	1.28e-06	4.98

TABLE 4.1
Accuracy table on non-uniform meshes in Sec. 4.1.1.

4.1.2. Accuracy test: nonlinear convection-diffusion equation. In this test, we solve the following nonlinear convection-diffusion equation to test the accuracy of our scheme for nonlinear problem:

$$u_t + f(u)_x = A(u)_{xx} + s(x,t), \tag{4.3}$$

where $f(u) = u^2/2$, $A(u) = \epsilon_d(u+1)^2$ and source term $s(x,t)$ aligned with the exact solution $u(x,t) = \exp(-\epsilon_d t)\sin(x-t)$ with $\epsilon_d = 10^{-3}$. The initial condition is taken as $u_0(x) = u(x,0)$ and the boundary condition is periodic. We compute the solution up to $T = 1$ on non-uniform meshes. The numerical results on non-uniform meshes are shown in Table. 4.2 and illustrate the optimal order of accuracy of our scheme.

N	L^1 Error	Order	L^2 Error	Order	L^∞ Error	Order
40	4.25e-02	–	2.18e-02	–	2.86e-02	–
80	1.50e-03	4.62	8.05e-04	4.56	1.12e-03	4.48
160	4.63e-05	4.89	2.51e-05	4.88	3.55e-05	4.85
320	1.42e-06	4.96	7.59e-07	4.98	1.07e-06	4.99

TABLE 4.2
Accuracy table on non-uniform meshes in Sec. 4.1.2.

4.1.3. Porous medium type equations. In this test, we consider the following porous medium type equations:

$$u_t = (a(u)u_x)_x, \tag{4.4}$$

with different diffusion coefficient $a(u)$ and different initial and boundary conditions. We first consider the Barenblatt solutions (see e.g., [23]) which has the exact solution

$B_{m,1}(x,t) = t^{-\kappa}\left[\left(1 - \frac{\kappa(m-1)}{2m}\frac{|x|}{2}\right)\right]^{1/(m-1)}$ with $u_+ = \max(u,0)$ and $\kappa = \frac{1}{m+1}$. For Barenblatt solutions, $a(u)$ is taken as mu^{m-1} with a positive integer m, the boundary condition is set to periodic boundary condition and the initial condition is set to $u_0(x) = B_{m,1}(x,1)$. We compute the solution up to $T = 2$ with $m = 2,3,5,8$, separately. The degeneracy for such problem occurs when $u = 0$. The numerical results are shown in Fig. 4.1 and agree well with the exact solutions. Next we test

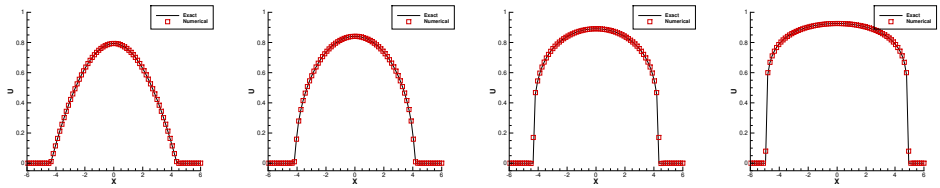

(a) m=2 (b) m=3 (c) m=5 (d) m=8

FIG. 4.1. *Numerical solution of 1D Barenblatt solutions on* 80 *non-uniform cells with* $m = 2,3,5,8$ *in Sec. 4.1.3.*

a named Marshak equation, introduced in [11, 13, 14], which serves as a benchmark demonstrating that certain numerical schemes may converge to an incorrect solution. This problem is set as $a(u) = u^3$ and has an exact solution [15]:

$$u(x,t) = \begin{cases} (3c(ct-x))^{1/3}, & \text{if } x < ct, \\ 0, & \text{otherwise,} \end{cases} \tag{4.5}$$

where c is taken as 0.4. The computational domain Ω is set as $[0,1]$ and the initial condition is taken as $u_0(x) = u(x,0)$. We set the left boundary as a time-dependent Dirichlet condition $u_L(t) = u(0,t)$ and a constant condition $u_R = 0$ on the right side of Ω. The numerical solution at $T = 2$ is presented in Fig. 4.2(a) and shows that our scheme aligns well with the exact solution.

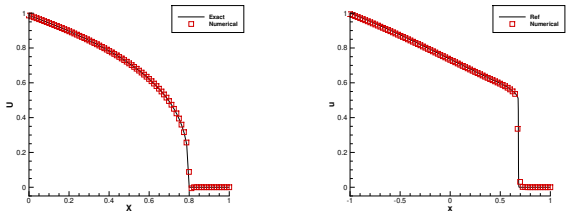

(a) Marshak equation in Sec. 4.1.3 at $T = 2$

(b) Strongly degenerate problems in Sec. 4.1.4 at $T = 1$

FIG. 4.2. *Numerical solutions of the Marshak equation in Sec. 4.1.3 and the strongly degenerate convection-diffusion equation in Sec. 4.1.4 on* 80 *non-uniform cells.*

4.1.4. Strongly degenerate convection-diffusion equation. In this test, we solve a strongly degenerate convection-diffusion equation which is firstly introduced in [6] to illustrate a numerical scheme may converge to an incorrect solution. The

equation is given as in (2.1) with the convective flux $f(u) = u^2/4$. The diffusion term $A(u)$ together with the initial data $u_0(x)$ in (2.1) are specified by

$$A(u) = \begin{cases} 0, \text{ if } u \le 0.5, \\ \frac{5}{4}(2u-1)^2, \text{ if } u \in (0.5, 0.6) \\ u - \frac{11}{20}, \text{ if } u \ge 0.6, \end{cases}, \quad u_0(x) = \begin{cases} 1, \text{ if } x \in [-1, -0.4), \\ -2.5x \text{ if } x \in [-0.4, 0), \\ 0, \text{ else.} \end{cases}$$

The boundary condition is set as Dirichlet condition: $u(-1,t) = 1$ and $u(1,t) = 0$. Here the term "strongly degenerate" refers to the fact that the set $\{u : A'(u) = 0\}$ has positive Lebesgue measure [20]. In this test, as there is no exact solution, the reference solution is obtained by applying a provably convergent scheme [6] on a mesh with $N = 1000$ uniform cells:

$$u_j^{n+1} = u_j^n + \frac{\Delta t}{\Delta x}\left(\hat{f}_{j+\frac{1}{2}} - \hat{f}_{j-\frac{1}{2}}\right) + \frac{\Delta t}{(\Delta x)^2}\left(A_{j+1}^n - 2A_j^n + A_{j-1}^n\right), \tag{4.6}$$

where u_j^n is the numerical solution approximating the point value $u(x_j, t_n)$, $\hat{f}_{j+\frac{1}{2}}$ is the Lax-Friedrichs flux defined in (2.9) and $A_j^n = A(u_j^n)$. The numerical solutions are presented in Fig. 4.2(b) and show that our scheme matches the reference solution well.

4.2. 2D numerical results. We present several two-dimensional tests, including accuracy tests, porous medium–type equations, anisotropic problems, problems on irregular domains, the Buckley–Leverett equation and the strongly degenerate convection–diffusion equation. The numerical results are all computed on unstructured triangular meshes, see e.g., Fig. 4.3.

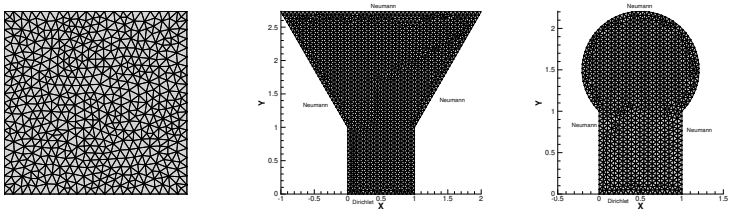

(a) Square domain (b) Square-trapezoidal domain (c) Square domain with a three-quarter disk

FIG. 4.3. *The unstructured triangular meshes used in Sec. 4.2.*

4.2.1. Accuracy test: linear convection-diffusion equation. We consider the linear convection-diffusion equation:

$$u_t + u_x + u_y = \epsilon_d(u_{xx} + u_{yy}), \tag{4.7}$$

with the exact solution $u(x,y,t) = \exp(-\epsilon_d t)\sin(x+y-2t)$, where ϵ_d is taken as 0.1. The initial condition is set as $u_0(x,y) = u(x,y,0)$ and the boundary condition is periodic. The computational domain Ω is taken as $[0, 2\pi] \times [0, 2\pi]$ and is decomposed into N pieces of triangles with maximum edge length $h_{\max}$. The final time is taken as 0.1 and the numerical results are shown in Table 4.3. The numerical result demonstrates that our scheme has optimal order of accuracy on unstructured triangular meshes.

N	$h_{\max}$	L^1 Error	Order	L^2 Error	Order	L^∞ Error	Order
551	4.48e-01	2.71e-02	–	2.98e-02	–	5.92e-02	–
2222	2.23e-01	2.01e-03	3.74	2.55e-03	3.54	7.90e-03	2.90
8616	1.16e-01	7.37e-05	5.02	9.69e-05	4.96	3.53e-04	4.72
19288	7.82e-02	1.01e-05	5.09	1.32e-05	5.11	4.86e-05	5.07

TABLE 4.3
Accuracy table for the 2D linear convection-diffusion equation (4.7) *in Sec. 4.2.1.*

4.2.2. Accuracy test: nonlinear convection-diffusion equation. In this test, we assess the accuracy of the proposed scheme for the following nonlinear convection–diffusion equation:

$$u_t + \left(\frac{u^2}{2}\right)_x + \left(\frac{u^2}{2}\right)_y = \epsilon_d \left((u^2)_{xx} + (u^2)_{yy}\right) + s_2(x,y,t), \tag{4.8}$$

where $\epsilon_d = 0.1$. The source term $s_2(x,y,t)$ is chosen such that the exact solution is $u(x,y,t) = exp(-\epsilon_d t)\sin(x+y-2t)$. The initial condition is chosen as $u_0(x,y) = u(x,y,0)$ and the boundary condition is periodic. The final time is taken as 0.1. All computational settings are the same as in Sec. 4.2.1. Table 4.4 reports the errors and the corresponding convergence rates, demonstrating the optimal order of accuracy.

N	$h_{\max}$	L^1 Error	Order	L^2 Error	Order	L^∞ Error	Order
551	4.48e-01	2.27e-02	–	2.54e-02	–	6.020e-02	–
2222	2.23e-01	1.85e-03	3.61	2.30e-03	3.46	7.23e-03	3.05
8616	1.16e-01	6.75e-05	5.03	8.62e-05	4.98	3.11e-04	4.78
19288	7.82e-02	9.38e-06	5.05	1.19e-05	5.07	4.05e-05	5.22

TABLE 4.4
Accuracy table for the 2D nonlinear convection-diffusion equation (4.8) *in Sec. 4.2.2.*

4.2.3. Accuracy test: anisotropic diffusion equation. In this test, we consider the following anisotropic diffusion equation:

$$u_t = \nabla^2 : \begin{pmatrix} 2u & 1.5u \\ 1.5u & 3u \end{pmatrix}, \tag{4.9}$$

with the initial condition $u(x,y,0) = \cos(y)\cos(2x-y)$ and the periodic boundary condition. This problem admits the exact solution $u(x,y,t) = \exp(-8t)\cos(y)\cos(2x-y)$. The final time is taken as 0.1 and the computational domain is the same as in the previous test. The numerical results are shown in Table 4.5 and demonstrates the optimal order of accuracy of our scheme for anisotropic problems.

N	$h_{\max}$	L^1 Error	Order	L^2 Error	Order	L^∞ Error	Order
551	4.48e-01	3.17e-03	2.96	4.42e-03	2.73	2.49e-02	1.39
2222	2.23e-01	1.12e-04	4.80	1.57e-04	4.80	1.12e-03	4.46
8616	1.16e-01	2.72e-06	5.65	3.70e-06	5.69	3.01e-05	5.49
19288	7.8e-02	2.50e-07	6.10	3.52e-07	6.02	3.84e-06	5.27

TABLE 4.5
Accuracy table for the 2D anisotropic diffusion equation (4.9) *in Sec. 4.2.3.*

4.2.4. PMEs: Barenblatt solution. The PME is given as:

$$u_t = (u^m)_{xx} + (u^m)_{yy}, \tag{4.10}$$

with different positive integers m and different initial conditions. Except for Sec. 4.2.6, the boundary conditions are all set as periodic boundary condition. Firstly, we test the Barenblatt solution, with the exact solution [3]:

$$B_{m,2}(x,y,t) = (t+1)^{-\kappa}\left(C_B - \frac{\kappa(m-1)}{4m}\frac{(|x|^2+|y|^2)}{(t+1)^{\kappa}}\right)_+^{1/(m-1)}, \ C_B = 0.1, \tag{4.11}$$

where $\kappa = \frac{1}{m}$. We take $u_0(x,y) = B_{m,2}(x,y,0)$ and evolve the solution up to $T = 4$ on the computational domain $\Omega = [-2,2]\times[-2,2]$, which is discretized by an unstructured triangular mesh consisting of 9362 elements with maximum edge length $h_{\max} \approx 0.098$. We report the numerical results at $T = 1, 2$ and 4. The results for $m = 2$ are shown in Fig. 4.4, while those for $m = 5$ are presented in Fig. 4.5. The numerical results indicate that the proposed scheme maintains relatively low errors on a coarse mesh.

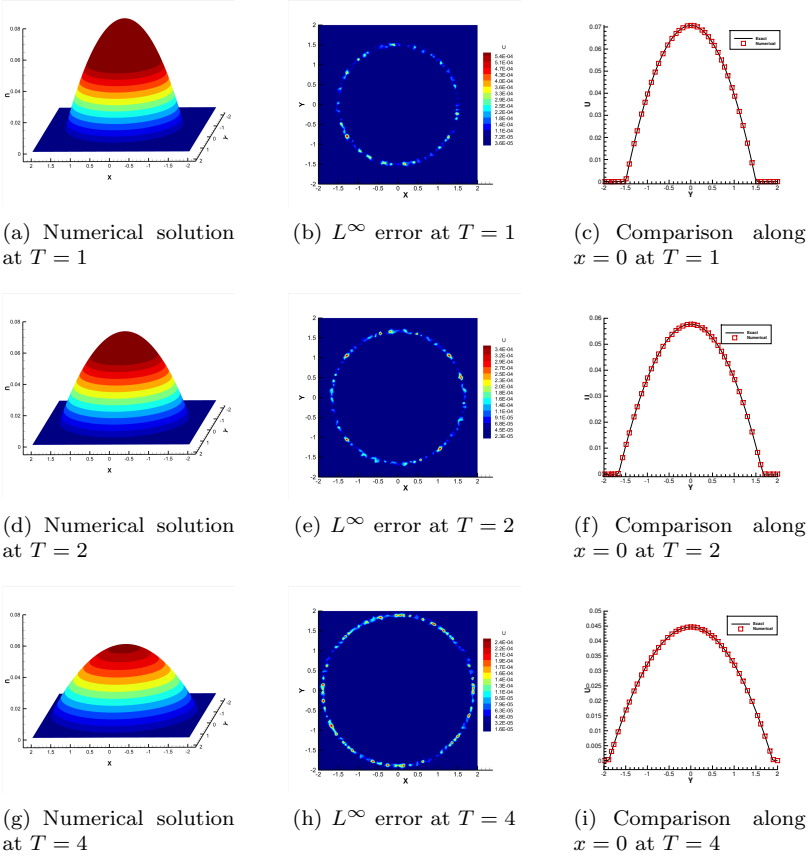

(a) Numerical solution at $T = 1$ (b) L^∞ error at $T = 1$ (c) Comparison along $x = 0$ at $T = 1$

(d) Numerical solution at $T = 2$ (e) L^∞ error at $T = 2$ (f) Comparison along $x = 0$ at $T = 2$

(g) Numerical solution at $T = 4$ (h) L^∞ error at $T = 4$ (i) Comparison along $x = 0$ at $T = 4$

FIG. 4.4. *Numerical solution of 2D Barenblatt solution on an unstructured triangular mesh with $m = 2$ in Sec. 4.2.4.*

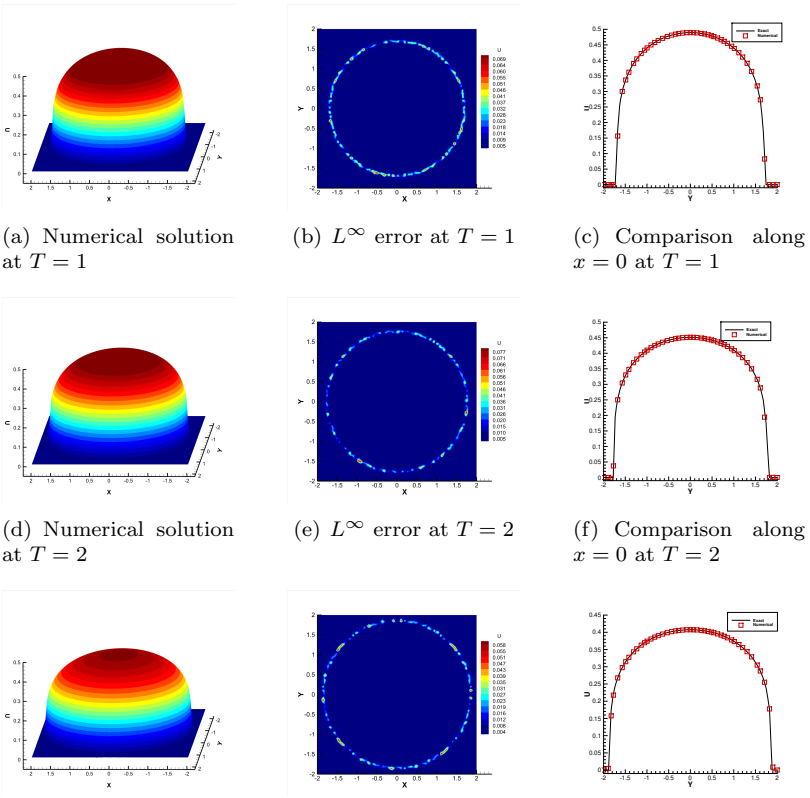

(a) Numerical solution at $T = 1$ (b) L^∞ error at $T = 1$ (c) Comparison along $x = 0$ at $T = 1$

(d) Numerical solution at $T = 2$ (e) L^∞ error at $T = 2$ (f) Comparison along $x = 0$ at $T = 2$

(g) Numerical solution at $T = 4$ (h) L^∞ error at $T = 4$ (i) Comparison along $x = 0$ at $T = 4$

FIG. 4.5. *Numerical solution of 2D Barenblatt solution on an unstructured triangular mesh with $m = 5$ in Sec. 4.2.4.*

4.2.5. PMEs: merging problem and discontinuous initial condition. In this test, we consider $m = 2$ in (4.10) with two different initial conditions. The first test is a merging problem, which illustrates the interaction and eventual merging of two compactly supported functions. The boundary condition is periodic and the initial condition is prescribed as:

$$u_0(x,y) = \begin{cases} \exp\left(\dfrac{-1}{6-(x-2)^2-(y+2)^2}\right), & (x-2)^2+(y+2)^2 < 6, \\ \exp\left(\dfrac{-1}{6-(x+2)^2-(y-2)^2}\right), & (x+2)^2+(y-2)^2 < 6, \\ 0, & \text{otherwise.} \end{cases} \tag{4.12}$$

For the merging test, we take the computational domain $\Omega = [-10, 10] \times [-10, 10]$. The numerical solutions at $T = 0.5, 1$, and 4 are shown in Fig. 4.6 and align well with the reference results reported in [8, 12, 21].

The second test uses discontinuous initial data:

$$u_0(x,y) = \begin{cases} 1, & \text{if } |x| \le 1 \text{ and } |y| \le 1, \\ 0, & \text{otherwise.} \end{cases} \tag{4.13}$$

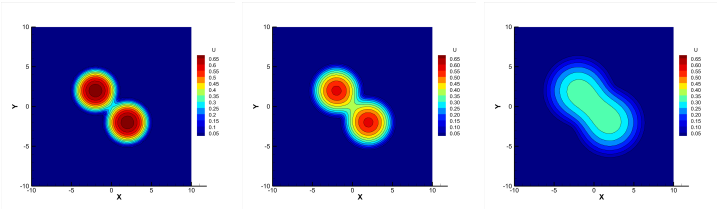

(a) Contour at $T = 0.5$ (b) Contour at $T = 1$ (c) Contour at $T = 4$

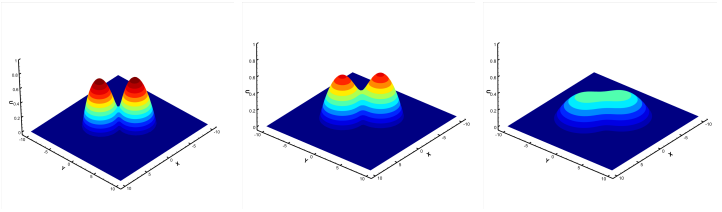

(d) Surface at $T = 0.5$ (e) Surface at $T = 1$ (f) Surface at $T = 4$

FIG. 4.6. *Numerical solutions at* $T = 0.5, 1, 4$ *for merging problems in Sec. 4.2.5 on* 9370 *unstructured triangles.*

The computational domain is $\Omega = [-2, 2] \times [-2, 2]$. This example is designed to test the robustness of the proposed DoC-FV scheme. We observe that, under the same settings, the DoC-LDG scheme proposed in [22] will blow-up for this test, while the present DoC-FV scheme performs well. For this second test, we utilize the following monotone finite difference method on a 1000×1000 uniform Cartesian mesh which is proved the semi-discrete convergence in [10]:

$$\frac{u_{ij}^{n+1} - u_{ij}^{n}}{\Delta t} = \frac{\left(A_{i+1,j}^{n} - 2A_{ij}^{n} + A_{i-1,j}^{n}\right)}{(\Delta x)^2} + \frac{\left(A_{i,j+1}^{n} - 2A_{ij}^{n} + A_{i,j-1}^{n}\right)}{(\Delta y)^2}, \tag{4.14}$$

where u_{ij}^{n} is an approximation of the exact $u(x_i, y_j, t^n)$ and $A_{ij}^{n} \triangleq (u_{ij}^{n})^2$. The numerical and reference solutions are shown in Fig. 4.7 and the results show that our scheme align well with the reference solution.

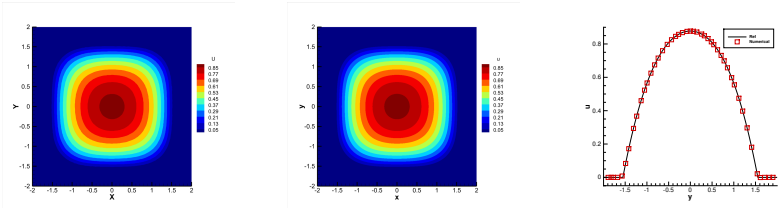

(a) Numerical solution (b) Reference solution (c) Comparison along $x = 0$

FIG. 4.7. *Numerical solutions of PME* (4.10) *with* $m = 2$ *and discontinuous initial condition at* $T = 0.1$ *in Sec. 4.2.5.*

4.2.6. PMEs: irregular domains. In this test, we consider the PME (4.10) on two nonstandard domains defined as the union of a square with (i) a trapezoid with $m = 2$ and (ii) a three-quarter disk with $m = 4$; see Fig. 4.3 for an illustration. The

boundary condition is set as the Dirichlet condition $u_B = 1$ at the bottom $y = 0$ and homogeneous Neumann condition $mu^{m-1}\nabla u \cdot \mathbf{n}_{\partial\Omega} = 0$ at other boundaries, where $\mathbf{n}_{\partial\Omega}$ is the outer normal vector of $\partial\Omega$. The boundary condition is also illustrated in Fig. 4.3(b) and Fig. 4.3(c). The initial condition is $u_0(x, y) = 1$ for $y < 1$ and $u_0(x, y) = 0$ otherwise. The numerical solutions computed on meshes in Fig. 4.3 and on refined meshes (used here as a reference) are shown in Fig. 4.8 and Fig. 4.9 for comparison. The numerical solutions on coarse meshes match the reference solutions well. We observe that, in the square-three-quarter-disk case (Fig. 4.9), the propagating front is not perfectly smooth; a similar behavior is also observed for the first-order scheme. This feature is likely caused by geometric discretization errors, since the circular arc is approximated by piecewise linear boundary segments on the unstructured triangular mesh. The artifact will gradually diminish under mesh refinement, and in contrast, no such artifact is observed in the square-trapezoid case (Fig. 4.8), where the boundary is polygonal and can therefore be fitted exactly by the mesh.

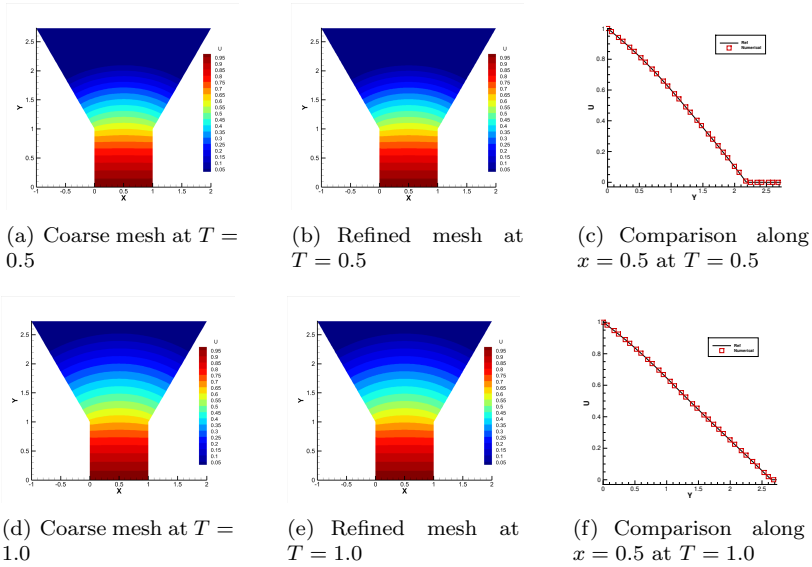

(a) Coarse mesh at $T = 0.5$

(b) Refined mesh at $T = 0.5$

(c) Comparison along $x = 0.5$ at $T = 0.5$

(d) Coarse mesh at $T = 1.0$

(e) Refined mesh at $T = 1.0$

(f) Comparison along $x = 0.5$ at $T = 1.0$

FIG. 4.8. *The numerical results of the PME with $m = 2$ on a square-trapezoid domain at $T = 0.5$ and $T = 1.0$ in Sec. 4.2.6 on both a coarse mesh (*3196 *triangles) and a refined mesh (*12118 *triangles).*

4.2.7. PMEs: anisotropic diffusion. In this test, we consider an anisotropic porous medium type equation as follows:

$$u_t = \sum_{i_1=1}^{2}\sum_{i_2=1}^{2} \partial_{i_1}\partial_{i_2} A(u), \tag{4.15}$$

with periodic boundary condition, where $A(u) = u^3/2$, ∂_1 represents ∂_x and ∂_2 represents ∂_y. The initial condition is taken as the discontinuous function (4.13) and the domain is set as $\Omega = [-2, 2] \times [-2, 2]$. The diffusion matrix of this equation is $A'(u)\begin{pmatrix} 1 & 1 \\ 1 & 1 \end{pmatrix}$ which makes this equation degenerate everywhere as the diffusion matrix always has a zero eigenvalue 0, and even two zero eigenvalues when $A'(u) = 0$.

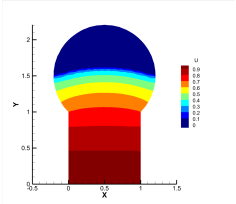

(a) Coarse mesh at $T = 0.4$

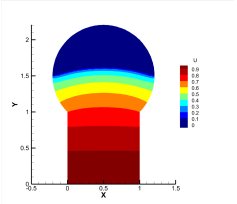

(b) Refined mesh at $T = 0.4$

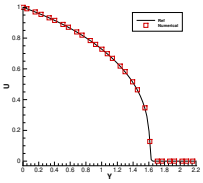

(c) Comparison along $x = 0.5$ at $T = 0.4$

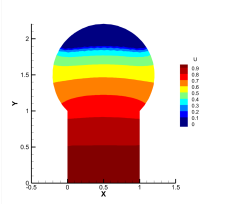

(d) Coarse mesh at $T = 0.$

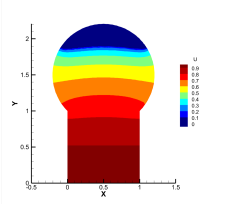

(e) Refined mesh at $T = 0.8$

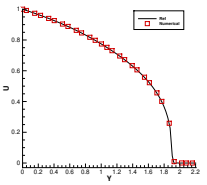

(f) Comparison along $x = 0.5$ at $T = 0.8$

FIG. 4.9. *The numerical results of the PME with $m = 4$ on a square-three-quarter-disk domain at $T = 0.4$ and $T = 0.8$ in Sec. 4.2.6 on both a coarse mesh (2058 triangles) and a refined mesh (5680 triangles).*

The everywhere-degeneracy makes this problem more challenging. The reference solution is computed using the following monotone finite difference scheme:

$$u_{ij}^{n+1} = u_{ij}^{n} + \frac{\Delta t}{(\Delta x)^2}\left(A_{i+1,j+1}^{n} - 2A_{ij}^{n} + A_{i-1,j-1}^{n}\right), \tag{4.16}$$

on 1000×1000 uniform rectangular meshes with mesh size $\Delta x = \Delta y = 1/250$, where u_{ij}^n is the point value and $A_{ij}^n = A(u_{ij}^n)$. The numerical solution and its comparison with the reference solutions are presented in Fig. 4.10, showing good agreement.

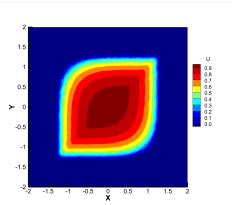

(a) Numerical solution

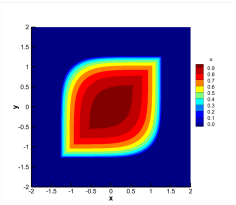

(b) Reference solution

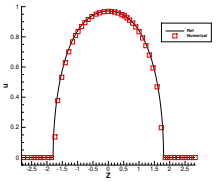

(c) Comparison along the diagonal $x = y$, plotted versus $z = \sqrt{x^2 + y^2}$

FIG. 4.10. *Numerical solution of anisotropic porous medium type equation* (4.15) *on* 9362 *triangles with discontinuous initial condition at $T = 0.1$ in Sec. 4.2.7.*

4.2.8. Buckley-Leverett equation. Here, we consider the Buckley-Leverett equation which is used to simulate the two-phase flow in porous media:

$$u_t + f_1(u)_x + f_2(u)_y = \frac{1}{100}(u_{xx} + u_{yy}), \tag{4.17}$$

where the non-convex convective fluxes are given as $f_1(u) = \frac{u^2}{u^2+(1-u)^2}$ and $f_2(u) = (1-5(1-u)^2)f_1(u)$ in (4.17). The boundary condition is periodic and the initial condition is $u_0(x,y) = 1$ for $x^2+y^2 < \frac{1}{2}$ and 0 otherwise. The computational domain is set as $\Omega = [-1.5, 1.5] \times [-1.5, 1.5]$ and is decomposed into 38070 unstructured triangles. The numerical solution at $T = 0.5$ is shown in Fig. 4.11 and agrees well with the solution in, e.g., [8, 21].

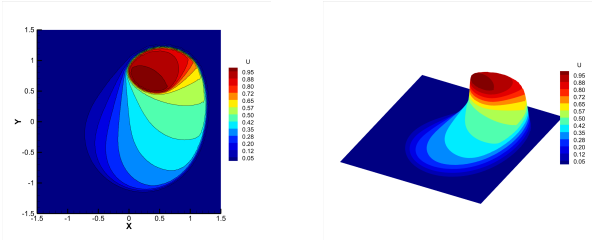

(a) Contour (b) Surface

FIG. 4.11. *Numerical solution of Buckley Leverett equation* (4.17) *in Sec. 4.2.8.*

4.2.9. Strongly degenerate convection-diffusion equation. In this test, we consider the following strongly degenerate convection-diffusion equation in two dimensions:

$$u_t + f_1(u)_x + f_2(u)_y = \epsilon_d(\nu(u)u_x)_x + \epsilon_d(\nu(u)u_y)_y, \tag{4.18}$$

where $f_1(u) = f_2(u) = u^2$, $\epsilon_d = 0.1$. The diffusion coefficient $\nu(u)$ and the initial condition are defined as:

$$\nu(u) = \begin{cases} 0, & |u| \le 0.25, \\ 1, & |u| > 0.25, \end{cases} \qquad u_0(x,y) = \begin{cases} 1, & (x+0.5)^2 + (y+0.5)^2 < 0.16, \\ -1, & (x-0.5)^2 + (y-0.5)^2 < 0.16, \\ 0, & \text{otherwise.} \end{cases} \tag{4.19}$$

The boundary condition is set as periodic condition. The computational domain is set as $\Omega = [-1.5, 1.5] \times [-1.5, 1.5]$ and is decomposed into 38070 unstructured triangles. The numerical solution at $T = 0.5$ is shown in Fig. 4.12 and matches well the solutions in, e.g., [8, 12, 21].

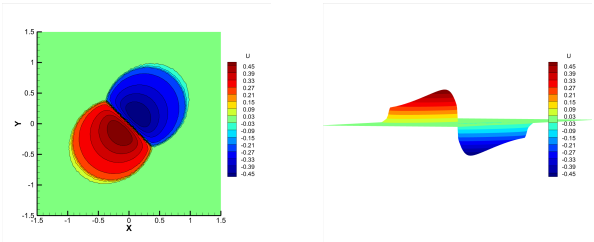

(a) Contour (b) Surface

FIG. 4.12. *Numerical solution of strongly degenerate convection-diffusion equation* (4.18) *in Sec. 4.2.9.*

5. Concluding remarks. In this work, we extend the notion of "double conservation" to unstructured triangular meshes, thereby removing a key obstacle to applying the DoC-FV scheme on general meshes. Building on this framework, we develop a DoC-FV scheme on non-uniform meshes in one dimension and on unstructured triangular meshes in two dimensions. To get the doubly conservative property, we introduce a new decomposition of $\nabla\phi_j$, the gradient of the piecewise linear hat function, which preserves the required local conservation for the convective flux. Then we prove that our new DoC-FV scheme satisfies the Lax-Wendroff type theorem. Extensive numerical experiments verify the high-order accuracy, non-oscillation near shocks, and robustness of the proposed method on both regular and irregular geometries.

As the future work, we plan to extend the DoC-FV scheme to more complex systems, including the compressible Navier-Stokes equations.

REFERENCES

[1] M. Ahmat, S. Ni, M. Zhang, and Z. Zhao, *A sixth-order finite difference HWENO scheme for nonlinear degenerate parabolic equation*, Computers & Mathematics with Applications, **150** (2023), 196–210.

[2] P. Castillo, B. Cockburn, I. Perugia, and D. Schötzau, *An a priori error analysis of the local discontinuous Galerkin method for elliptic problems*, SIAM Journal on Numerical Analysis, **38** (2000), 1676–1706.

[3] Q. Cheng, Q. Liu, W. Chen, and J. Shen, *A new flow dynamic approach for Wasserstein gradient flows*, Journal of Computational Physics, **524** (2025), 113696.

[4] Y. Cheng and C.-W. Shu, *A discontinuous Galerkin finite element method for time dependent partial differential equations with higher order derivatives*, Mathematics of Computation, **77** (2008), 699–730.

[5] R. Díaz-Adame, S. Jerez, and H. Carrillo, *Fast and optimal WENO schemes for degenerate parabolic conservation laws*, Journal of Scientific Computing, **90** (2022), 22.

[6] S. Evje and K. H. Karlsen, *Monotone difference approximations of bv solutions to degenerate convection-diffusion equations*, SIAM Journal on Numerical Analysis, **37** (2000), 1838–1860.

[7] S. Gottlieb, C.-W. Shu, and E. Tadmor, *Strong stability-preserving high-order time discretization methods*, SIAM Review, **43** (2001), 89–112.

[8] Y. Jiang, *High order finite difference multi-resolution WENO method for nonlinear degenerate parabolic equations*, Journal of Scientific Computing, **86** (2021), 1–20.

[9] S. Y. Kadioglu, R. R. Nourgaliev, and V. A. Mousseau, *A comparative study of the harmonic and arithmetic averaging of diffusion coefficients for non-linear heat conduction problems*, Technique Report, Idaho National Laboratory, (2008).

[10] K. H. Karlsen, N. H. Risebro, and E. B. Storrøsten, *On the convergence rate of finite difference methods for degenerate convection-diffusion equations in several space dimensions*, ESAIM: Mathematical Modelling and Numerical Analysis, **50** (2016), 499–539.

[11] K. Lipnikov, G. Manzini, J. D. Moulton, and M. Shashkov, *The mimetic finite difference method for elliptic and parabolic problems with a staggered discretization of diffusion coefficient*, Journal of Computational Physics, **305** (2016), 111–126.

[12] Y. Liu, C.-W. Shu, and M. Zhang, *High order finite difference WENO schemes for nonlinear degenerate parabolic equations*, SIAM Journal on Scientific Computing, **33** (2011), 939–965.

[13] D. C. Maddix, L. Sampaio, and M. Gerritsen, *Numerical artifacts in the generalized porous medium equation: Why harmonic averaging itself is not to blame*, Journal of Computational Physics, **361** (2018), 280–298.

[14] V. Prakash K and G. Natarajan, *Revisiting numerical artifacts in the generalized porous medium equation with continuous coefficients: Does averaging really matter?*, Journal of Computational Physics, **537** (2025), 114101.

[15] A. A. Samarskii and I. M. Sobol, *Examples of the numerical calculation of temperature waves*, USSR Computational Mathematics and Mathematical Physics, **3** (1963), 945–970.

[16] C. Shi and C.-W. Shu, *On local conservation of numerical methods for conservation laws*, Computers & Fluids, **169** (2018), 3–9.

[17] C.-W. Shu, *Bound-preserving high order finite volume schemes for conservation laws and convection-diffusion equations*, in International Conference on Finite Volumes for Complex

Applications, Springer, 2017, 3–14.
[18] C.-W. Shu, *Essentially non-oscillatory and weighted essentially non-oscillatory schemes*, Acta Numerica, **29** (2020), 701–762.
[19] J. L. Vazquez, *The Porous Medium Equation: Mathematical Theory*, Oxford University Press, 2006.
[20] Z. Wu, J. Zhao, J. Yin, and H. Li, *Nonlinear diffusion equations*, World Scientific, 2001.
[21] Z. Xu and Y.-T. Zhang, *High-order exponential time differencing multi-resolution alternative finite difference WENO methods for nonlinear degenerate parabolic equations*, Journal of Computational Physics, **529** (2025), 113838.
[22] K. Yu, J. Cheng, Y. Liu, and C.-W. Shu, *A Lax-Wendroff type theorem of doubly conservative schemes for degenerate convection-diffusion equations*, Mathematics of Computation, to appear. DOI: https://doi.org/10.1090/mcom/4167 (2026).
[23] X. Zhang, Y. Liu, and C.-W. Shu, *Maximum-principle-satisfying high order finite volume weighted essentially nonoscillatory schemes for convection-diffusion equations*, SIAM Journal on Scientific Computing, **34** (2012), 627–658.
[24] X. Zhang, S. Su, and J. Wu, *A vertex-centered and positivity-preserving scheme for anisotropic diffusion problems on arbitrary polygonal grids*, Journal of Computational Physics, **344** (2017), 419–436.
[25] J. Zhu and C.-W. Shu, *A new type of multi-resolution WENO schemes with increasingly higher order of accuracy*, Journal of Computational Physics, **375** (2018), 659–683.
[26] J. Zhu and C.-W. Shu, *A new type of multi-resolution WENO schemes with increasingly higher order of accuracy on triangular meshes*, Journal of Computational Physics, **392** (2019), 19–33.